A scaling methodology for the Hybrid-Lambda Rotor - Characterization and validation in wind tunnel experiments

Daniel Ribnitzky[1,2], Vlaho Petrović[1,2], and Martin Kühn[1,2]

[1]Carl von Ossietzky Universität Oldenburg, School of Mathematics and Science, Institute of Physics
[2]ForWind - Center for Wind Energy Research, Küpkersweg 70, 26129 Oldenburg, Germany
Correspondence: Daniel Ribnitzky (daniel.ribnitzky@uol.de)

Abstract. The Hybrid-Lambda Rotor is an aerodynamic rotor concept that enables very low-specific-rating offshore wind turbines in order to increase the power output in light winds and to limit the loads on the very long and slender rotor blades in strong winds. In this paper, the rotor concept is scaled to wind tunnel size and validated under reproducible inflow conditions. The objectives are to derive a scaling methodology, to investigate the influence of the steep gradients of axial induction along the

5 blade span and to characterize the wake of the Hybrid-Lambda Rotor in wind tunnel experiments. The scaling objectives are to match the axial induction distribution and to incorporate the change in the angle of attack distribution when switching between the light-wind and strong-wind operating mode. The derived model rotor with a diameter of 1.8 m is experimentally investigated and compared to a conventional ~~model wind turbine~~ in the large turbulent wind tunnel in Oldenburg under tailored inflow conditions produced with an active grid. A two-dimensional Laser-Doppler-Anemometer is used to measure the axial induction

10 in the rotor plane and the wake is characterised by means of a hot-wire rig. The measurement data is supplemented with free-vortex-wake simulations ~~on~~ both rotors. The results demonstrate that switching the operating modes with the characteristic change in the angle of attack distribution, works similar for the model and the full-scale turbine. The strong gradients of axial induction along the blade span lead to complex three-dimensional flow structures such as an increased radial flow component in the rotor plane. The low-induction design of the outer part of the rotor reduces the load overshoots in gust events compared to

15 the conventional model turbine. The wake characterization reveals an outer annulus with reduced wake deficits, an additional shear layer and vortex system and overall reduced wake deficits over a wide range of wind speeds below rated power. The derived results help to understand the unique flow patterns that are introduced by the Hybrid-Lambda Rotor and provide a valuable complementary data set to the simulations on the full-scale rotor.

1 Introduction

20 The large scale employment of offshore wind energy is one of the main pillars to fight climate change. ~~But,~~ integrating more and more conventional wind turbines in the energy grid will lead to an oversupply of power feed-in during strong winds and a deficit ~~still remains~~ in light winds. This effect is often named self-cannibalization of wind energy (López Prol et al., 2020) as it is self-amplifying with the share of wind energy in the overall energy mix. It is further intensified by the effect of large cluster wakes which will significantly reduce the efficiency of many wind farms especially in light winds and in the context of limited

available offshore sites and very close spacing of wind farm clusters (Dörenkämper et al., 2023; Schneemann et al., 2020). Self-cannibalization leads to high prices of electricity during light-wind days and low to zero (or sometimes negative) ~~stock~~ prices during strong-wind days, as predicted by May et al. (2015) ~~already 10 years ago~~. Thus, there is a need for wind turbines that produce more power in light winds. Onshore, this aim is usually accomplished by ~~the~~ means of larger rotor diameters in relation to the rated power, i.e. so-called low-specific power (Swisher et al., 2022). The increasing length and mass of the

30 blades cause loads that are no longer technically feasible which consequently leads the design and control engineers to the need for load limiting techniques. The purpose is to reduce the extreme loads close to rated wind speed but ~~these techniques~~ come with a loss in aerodynamic efficiency and thus a reduced power ~~feed-in~~. Especially at offshore sites, this contradicts with the higher annual average wind speed since a large portion of the energy yield would be achieved in ~~regions~~ with reduced aerodynamic efficiency. There is a need for novel design and control methodologies that enable large offshore rotors with low-specific

35 ratings. Such concepts limit the power losses due to load limiting strategies, which can go hand in hand with techniques that reduce the wake losses.

For this purpose, the Hybrid-Lambda Rotor concept for offshore turbines was developed by Ribnitzky et al. (2024). It features a rotor design for two tip speed ratios (TSR) and a non-uniform axial induction distribution along the blade span. To limit

40 the loads, the blades are pitched towards feather before rated wind speed and in addition, the rotor is switched to a strong-wind mode. Here, the rotor is operated at a lower TSR and a lower axial induction, and the spanwise angle of attack distribution is ~~tilted~~ with a decreasing trend towards the blade tip. When limiting the loads to a certain constraint, this novel combination of blade design and control strategies was proven to cause lower losses in the power production compared to conventional blade designs and load limiting strategies, such as solely pitching the blades to feather.

45

In previous studies, Ribnitzky et al. (2022) investigated the rotor concept with standard simulation methodologies such as the blade element momentum (BEM) theory. This theory relies on the assumption of independent blade elements. The rotor design with the steep gradients of the axial induction distribution along the blade span consequently reaches the limits of the applicability of the BEM theory. In subsequent investigations, Ribnitzky et al. (2023) analysed the concept using free-vortex-wake

50 (FVW) and large-eddy simulations (LES) and the results where compared to the BEM theory. Although ~~an overall~~ reasonable agreement was found for rotor integrated quantities like power, thrust and blade root bending moment, discrepancies were noticed in the spanwise~~-~~resolved variables, like the axial induction and the angle of attack distribution. Those studies further revealed a second shear layer in the wake that is trailing from the mid-span blade region with the steep gradients. This opens interesting questions about the ~~impact on the~~ blade aerodynamics and the wake of such a rotor. To consolidate the findings

55 from the simulation-based studies, an experimental validation of the Hybrid-Lambda Rotor concept is lacking. This leads us to the question of how the rotor concept can be scaled to wind tunnel size.

Designing a model wind turbine blade for the use in a wind tunnel usually aims at replicating certain physical characteristics of a full-scale rotor. This process ~~is a delicate compromise finding~~ since an exact match of all relevant physical parameters

between the model and the full-scale turbine is usually not possible. Canet et al. (2021), Bottasso and Campagnolo (2021) and Gasch and Twele (2012) thoroughly analyse the scaling of wind turbines in general. Scaling the Hybrid-Lambda Rotor involves four major challenges. First, the large geometric scaling factor, second the high design TSR of 11 of the full-scale rotor, third the non-uniform distribution of the axial induction along the blade span and fourth the ability to change between a light-wind and a strong-wind operating mode. The first two aspects can lead to very low chord lengths which is a challenge for the manufacturability and which leads to very low Reynolds numbers. This would result in an undesired change in the airfoil polars and a loss in aerodynamic efficiency. The latter two aspects require a delicate blade design for two main operating conditions that can mimic the characteristics of the Hybrid-Lambda Rotor even in the small-scale environment of a wind tunnel. In this study, the emphasis is on the ~~aerodynamic effects~~. Consequently, the model blades are designed over-proportionally stiff to separate aerodynamic effects from aero-elastic interactions. Further, the design and application of a transient controller for the wind tunnel model ~~is~~ addressed in future studies.

Once successfully designed and manufactured, a wind tunnel model could provide valuable insights about the influence of the steep gradients of the axial induction along the blade span. It further allows to explore the possibilities of changing the operating modes and changing the spanwise angle of attack distribution and it enables an in-depth characterization of the wake of the Hybrid-Lambda Rotor. Wang et al. (2021) showed that wakes of scaled wind turbines can deliver a very good representation of the full-scale counterpart with minor exceptions due to nacelle effects in the inner near-wake region.

A non-uniform spanwise load distribution of the rotor can lead to an enhanced wake mixing, according to Kelley et al. (2014) and Yang et al. (2015). They investigated blade designs with larger spanwise gradients of bound circulation with FVW and LES simulations and found that those rotors exhibit shorter and faster mixing far wakes. Dong et al. (2023) compared the wake of rotors with different spanwise load distributions and found that the wake recovery rate is higher for a blade design with a load distribution that is shifted more towards the blade root. Low-specific-rating turbines that operate at lower thrust coefficients over a wide range of wind speeds can have additional advantages on a wind farm level ~~which was analysed by~~ Madsen et al. (2020). Further rotor concepts ~~are present~~ that aim ~~for enhancing~~ wake diffusion. Knauer (2021) introduced a rotor design with a nearly inverse axial induction distribution, compared to the Hybrid-Lambda Rotor. He used a ventilation area with negative axial induction close to the blade root, introducing a small jet of relatively high wind speeds into the rotational centre of the wake.

The overall objective of this paper is to experimentally characterize and validate the aerodynamic design concept of the Hybrid-Lambda Rotor under reproducible, turbulent and transient inflow conditions ~~on~~ wind tunnel ~~scale. More specific,~~ the contribution aims to (1) develop a method ~~on how~~ to scale the Hybrid-Lambda Rotor concept to wind tunnel size, (2) to investigate the influence of the steep gradients of axial induction along the blade span on the aerodynamics and (3) to characterize the near wake of the Hybrid-Lambda Rotor.

2   Scaling methodology of the Hybrid-Lambda Rotor

95   In this section, we scale the Hybrid-Lambda Rotor with a rated power of 15 MW and a diameter of 326 m (Ribnitzky et al., 2024) to the size of the Model Wind Turbine Oldenburg with a diameter of 1.8 m (MoWiTO 1.8). The model turbine is usually operated with a conventional set of blades, as described in Berger et al. (2018) and Berger et al. (2021). This rotor is an aerodynamically scaled version of the NREL 5 MW reference turbine, defined by Jonkman et al. (2009), scaled under the objective of maintaining the design TSR and the lift distribution along the blade span, and it will serve as a reference rotor for this study.

100

The scaling methodology for the Hybrid-Lambda Rotor presented here differs from the aforementioned scaling approach of the reference rotor. The Hybrid-Lambda design methodology, as described by Ribnitzky et al. (2024), aims at increasing the rotor diameter compared to a reference rotor in order to increase the power in light winds. In contrast, the scaling approach presented here aims at the same rotor diameter as the reference model turbine (1.8 m). This ensures similar boundary conditions in the wind tunnel among the two rotors, considering rotor aerodynamics and wake extension. Figure 1 gives an

105   overview of the scaling and design methodology. The most straight forward approach in deriving a scaled model would be a geometric downscaling of the full-scale blade. Scaling the Hybrid-Lambda Rotor from a diameter of 326 m to 1.8 m leads to a length scaling factor of $n_l = D_m/D_f = 1/181$, where D is the rotor diameter and the subscripts m and f refer to the model turbine and full-scale turbine, respectively. An exact geometric downscaling would lead to a chord length at the tip of

110   only 8 mm and an unfeasibly low blade thickness of 0.8 mm. Further, if the internal blade shape would be scaled exactly, this would lead to a blade mass of only 24 g and a tip deflection under rated conditions of 14 cm. Clearly, these values illustrate that a geometrical downscaling is not an option. Beside manufacturing constraints, the short chord length would lead to very low Reynolds numbers of about 37000 at the blade tip at rated power, resulting in non-negligible changes in the airfoil polars and unacceptable losses in the aerodynamic efficiency. Consequently, an aerodynamic redesign of the blade is necessary. This

115   means, a new blade shape is defined that matches some pre-defined characteristics of the full-scale rotor. Choosing different airfoils and a new chord and twist distribution leads to a visually different blade which is, however, completely irrelevant as long as the relevant aerodynamic properties are reasonably matched. The first step is to properly define the scaling objectives and to choose the aerodynamic characteristics that should be matched, since as previously mentioned, not all characteristics can be fulfilled at the same time.

120

Common scaling approaches aim for replicating the TSR and the non-dimensional spanwise circulation distribution. However, the aforementioned challenges forced us to partially deviate from this approach. In contrast, in this study we focused on matching the axial induction distribution along the blade span for the light-wind and strong-wind operating modes of the full-scale Hybrid-Lambda Rotor and we adapted the operational TSRs. Further, we aimed ~~on incorporating the possibility to~~

125   ~~change the~~ operating mode and consequently to tilt the angle of attack distribution similar as to the full-scale rotor. More precisely, tilting the angle of attack distribution during the transition from the light-wind mode to the strong-wind mode means that the angle of attack is lowered in the outer part of the blade, but increased for the inner part. With the focus on aerody-
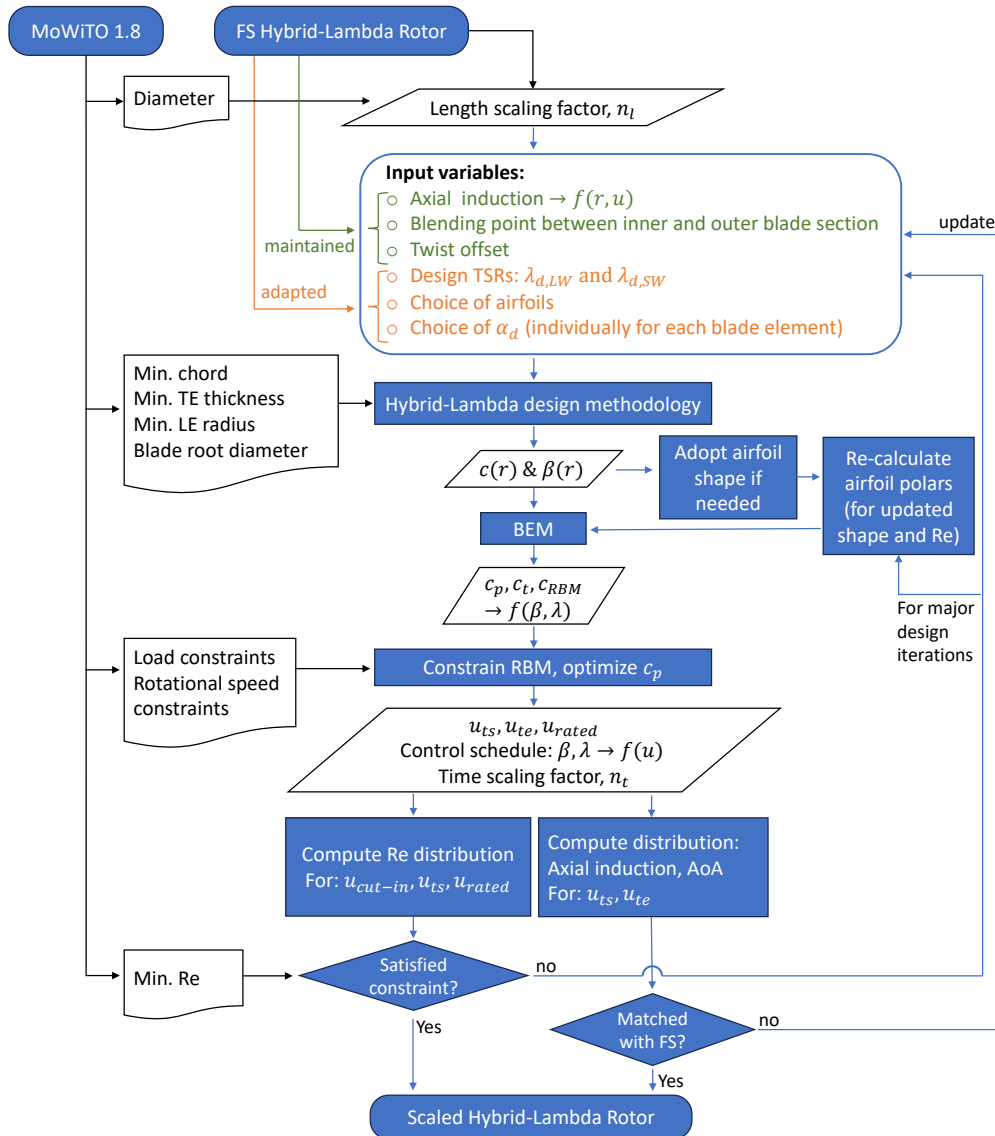
Figure 1. Scaling and design workflow for the Hybrid-Lambda Rotor. FS, full-scale; LW, light wind; SW, strong wind; AoA, angle of attack; $f(\ldots)$, as a function of $(\ldots)$

namic investigations, we decided to design the model blades over-proportionally stiff in order to exclude elastic effects and unintended fluid-structure interactions that could overshadow fundamental effects resulting solely from the novel blade design

130   methodology.

An application of the design TSRs of 11 and 9 from the full-scale rotor is not feasible for the wind tunnel size, as the derived chord lengths and local Reynolds number would be too low, even with the choice of new airfoils. The Reynolds number (Re) is defined by Eq. 1.

$$\text{Re} = \frac{c \cdot u_{\text{rel}} \cdot \rho}{\eta} \tag{1}$$

Here, ρ is the air density and η is the dynamic viscosity which are both usually constant across full-scale and wind tunnel applications. The relative velocity at the respective blade element u_{rel} is proportional to the inflow velocity u_∞ and the design TSR λ_{d}, as denoted in Eq. 2. The characteristic length c is the chord length which follows the trends as expressed in Eq. 3, according to a Betz blade design as described by Gasch and Twele (2012). Here, *R* is the rotor radius, *B* is the number of blades and $C_{\text{l,d}}$ is the design lift coefficient. Consequently, Re scales with the reciprocal of λ_{d}, as denoted in Eq. 4 and larger Reynolds numbers can be achieved by reducing the design TSR and choosing a low design lift coefficient.

$$u_{\text{rel}} \propto \lambda_{\text{d}} \cdot u_\infty \tag{2}$$

$$c \propto \frac{R}{B \cdot \lambda_{\text{d}}^2 \cdot C_{\text{l,d}}} \tag{3}$$

$$\text{Re} \propto \frac{R \cdot u_\infty}{\lambda_{\text{d}} \cdot B \cdot C_{\text{l,d}}} \tag{4}$$

The design TSRs from state of the art model wind turbines range from 4.5 to 7.5. Examples include model wind turbines that are scaled for aero-servo (and potentially elastic) investigations, as the MoWiTO 1.8 (Berger et al., 2018), the TU Munich G2 (Bottasso et al., 2014) and the Polimi model turbine (Bayati et al., 2016) with a design TSR of 7.5. Model turbines that are designed for wake (and potentially wind farm) investigations are the TU Munich G1 (Campagnolo et al., 2016) with a design TSR of 7, the NTNU (Krogstad and Lund, 2012) and the MoWiTO 0.6 (Schottler et al., 2016) with a design TSR of 6. Even lower design TSRs of 5 and 4.5 are chosen for model turbines with smart blade applications, as the TU Delft (Hulskamp et al., 2011) and the TU Berlin (BeRT) (Soto-Valle et al., 2020) turbines. Also models with large diameters, like the MEXICO rotor (Schepers and Snel, 2008) or the NREL phase VI turbine (Hand et al., 2001), with diameters of 4.5 m and 10 m, were designed for relatively low TSRs of 6.7 and 5.4, respectively.

Consequently, we decided to reduce the design TSRs of the Hybrid-Lambda Rotor for the wind tunnel model. Within the iterative design process, several TSRs were investigated. We found that a design TSR for the light-wind mode $\lambda_{\text{d,LW}} = 7.5$ works well in order to fulfil the constraints of minimal chord length and Reynolds number. Further, there is the advantage of the comparability with the conventional blades for the MoWiTO 1.8, as they feature a design TSR of 7.5, too. The design TSR for the strong-wind mode $\lambda_{\text{d,SW}}$ was chosen in order to incorporate a similar change in the inflow angle distribution as ~~compared~~

to the full-scale rotor when switching from light-wind to strong-wind mode. The aforementioned change can be calculated with Eq. 5 and is visualized in Fig. 2, using the axial induction distribution from the full-scale rotor (a_{SW} and a_{LW}).

$$\Delta\phi(r) = \arctan\left((1 - a_{\text{SW}}(r))\frac{R}{r \cdot \lambda_{\text{d,SW}}}\right) - \arctan\left((1 - a_{\text{LW}}(r))\frac{R}{r \cdot \lambda_{\text{d,LW}}}\right) \tag{5}$$
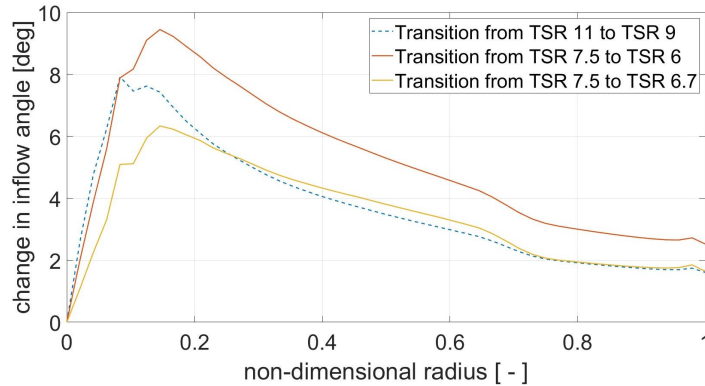
Figure 2. Change in the inflow angle distribution for operational transition of TSRs, full-scale rotor represented with dashed line

165

It can be readily seen, that a reduction of the TSR from 7.5 to 6.7 would lead to a similar change in the inflow angle compared to a reduction from 11 to 9 (as for the full-scale rotor) in the relevant blade region, except for the segments close to the blade root. However, we chose the strong-wind TSR to be 6 for two reasons. First, we want to enlarge the effect of the change in the angle of attack distribution in order to facilitate the measurability with the background of measurement uncertainties. Second,

170 this widens up the wind speed range where the transition between the light-wind and the strong-wind mode happens, which opens up more opportunities for control-related investigations in the wind tunnel.

The next step in the design process is the choice of airfoils. We investigated several low-Reynolds number airfoils and decided to use the SG6040 and SG6041 airfoils (Giguere and Selig, 1998) which were also used for the conventional blades of

175 the MoWiTO 1.8, for the sake of comparability. The polars are simulated with XFoil for the individual blade element with the respective Reynolds number with a N_{crit} value of 7 and without a forced transition. N_{crit} is the critical amplification factor that describes the transition between laminar and turbulent flow over the airfoil.

With the choice of design TSRs and airfoils being made, the design process continues with the application of the Hybrid-

180 Lambda design methodology. However, certain constraints need to be taken into account. The Reynolds number should be at least 70000 as suggested by Bottasso and Campagnolo (2021) to limit the reduction in aerodynamic efficiency. The chord length directly influences the Reynolds number. In addition, the constraint of the minimal chord length due to manufacturing reasons is set to 3 cm. This is not a strict limit, but it is related to the minimal leading edge radius and the minimal trailing

edge thickness of 0.5 mm within the milling process of the blade mould. The smaller the chord length is, the larger are the
adjustments that need to be applied to the airfoil shape in order to maintain the constraints for the leading edge radius and
trailing edge thickness. The blade root diameter is constrained to 35 mm in order to include the same pitch actuation mecha-
nism and the same blade root connection to the hub as it is used for the conventional blades. In theory, the maximum flapwise
blade root bending moment (RBM) scales with n_l^3 which would result in a value of 10.6 Nm for the wind tunnel model. This
is the load level where the transition from light-wind to strong-wind mode takes place in a steady-state assumption. However,
under transient inflow conditions higher loads are expected. Due to load limiting constraints of the MoWiTO 1.8, we lowered
the design value for the steady-state maximum flapwise RBM to 7.5 Nm. The operational range of the rotational speed must
be between 420 rpm and 600 rpm. It is constrained by the first tower eigenfrequency at the lower end and by the maximum
rotational speed of the slip ring in the drive train at the upper end.

Next, the Hybrid-Lambda design methodology, as described by Ribnitzky et al. (2024), is applied with the following input
variables. The design TSRs are set to 7.5 and 6, as explained above. Identical to the full-scale rotor, the blending region be-
tween the inner and outer blade section is set to 70% blade length (equivalent to 73% rotor radius for the model turbine) and
the twist offset for the inner blade region is set to $-2.5°$. Further information on the twist offset within the Hybrid-Lambda
design methodology is given by Ribnitzky et al. (2024). The desired axial induction distribution is adopted from the full-scale
rotor, since this is the major scaling objective. The design angle of attack (α_d) is derived from a compromise ~~finding~~ between
achieving good lift-to-drag ratios ($\alpha_{\mathrm{max,L/D}} \approx 4.5°$), maintaining reasonable margins to the stall region ($\alpha_{\mathrm{stall}} \approx 11.5°$) and
maintaining low lift coefficients that help to fulfil the minimum Reynolds number and chord length constraints. Consequently,
the design angle of attack is set close to the maximum lift-to-drag ratio for the inner part of the blade where the low design
TSR already ensures large enough chord lengths. For the outer part of the blade, the design angle of attack is reduced in order
to enlarge the chord length which also matches well with the angle of attack distribution of the full-scale rotor. With these input
variables, the chord and twist distribution can be calculated. Those are shown in Fig. 3 for the final blade design.

BEM simulations with steady and uniform inflow provide the aerodynamic performance curves, such as the power coefficient
c_{p}, thrust coefficient c_{T} and flapwise RBM as a function of pitch angle β, and operational TSR. Now, the constraint of flapwise
RBM is applied and the wind speed is calculated at which the limiting loads are reached. This leads to the control strategy, e.g.
rotational speed and pitch angle over wind speed, as shown in Fig. 4 for the final scaled design. Now, the wind speed at which
the transition to the strong-wind mode starts, u_{ts}, and when it ends, u_{te}, are known, as well as the respective pitch angles. With
the rotational speed at u_{ts}, we can also calculate the time scaling factor which we define as

$$n_t = t_m/t_f = \omega_{\mathrm{trans,f}}/\omega_{\mathrm{trans,m}} = 1/114. \tag{6}$$

Using the maximum rotational speed of 600 rpm would lead to a similar time scaling factor but since most of the measurements
are performed at ω_{trans} we will define the time scaling in this operating point. An overview of the actual turbine parameters
and the scaling factors is provided in Table 1. Note, that since we transferred the Hybrid-Lambda concept to lower TSRs, the

scaling of the wind speed, which would be defined as n_l/n_t does not hold true in this case. However, if we define the scaling ratios of the design TSRs as

220   $n_{\lambda,LW} = \lambda_{\text{LW,m}}/\lambda_{\text{LW,f}}$ and $n_{\lambda,SW} = \lambda_{\text{SW,m}}/\lambda_{\text{SW,f}}$ (7)

respectively, the wind speeds can be derived from Eq. 8 and 9:

$$u_{\text{ts,m}} = u_{\text{ts,f}} \cdot \frac{n_l}{n_t \cdot n_{\lambda,LW}}$$ (8)

$$u_{\text{te,m}} = u_{\text{te,f}} \cdot \frac{n_l}{n_t \cdot n_{\lambda,SW}}$$ (9)

225   Finally, we can check the angle of attack and axial induction distribution for the two operating points (u_{ts} and u_{te}), as shown in Fig. 6, and we can verify the scaling objectives. Is the axial induction distribution from the full-scale rotor reasonably matched? Is the change in the angle of attack distribution reasonable when switching the operating modes? Is the constraint for the Reynolds number achieved (see Fig. 5)? The design optimization loop is closed by re-tuning the input parameters and calculating the next design iteration. For major design updates, we re-calculate the airfoil polars as follows. The minimum

230   leading edge radius and trailing edge thickness is constrained due to manufacturing reasons. Consequently, the airfoil shape needs to be adapted for all blade elements where the derived chord length would lead to a violation of the constraints. Now, that the relative velocity at the respective blade element is known from the BEM simulations, the airfoil polars can be re-calculated for each individual blade element, considering the expected Reynolds number and the modified airfoil shape. The largest adaptation to the airfoil shape is necessary for the blade element with the shortest chord length, consequently at the blade

235   tip. We observed an increase in the drag coefficient for angles of attack greater than $3.5°$ which results in a reduction in the maximum lift-to-drag ratio by 15% compared to the unchanged airfoil. These numbers highlight the importance of considering the modifications to the airfoil shape, since the effect is happening in the relevant region of operational angle of attacks.
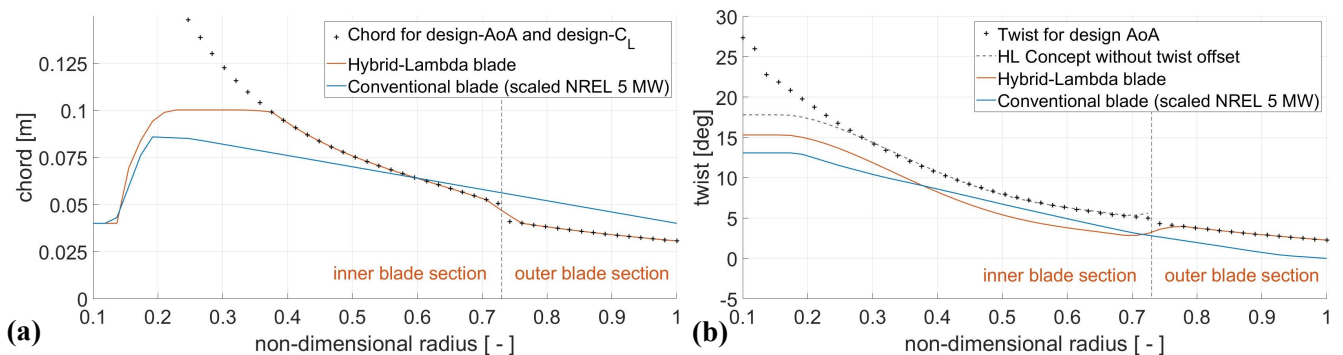
Figure 3. Chord (a) and twist distribution (b) for the scaled Hybrid-Lambda Rotor and the scaled NREL 5MW turbine

Figure 5. Reynolds number for three different operating modes, derived from BEM simulations

Figure 4. Control schedule for the Hybrid-Lambda model turbine (HL MT), derived from BEM simulations
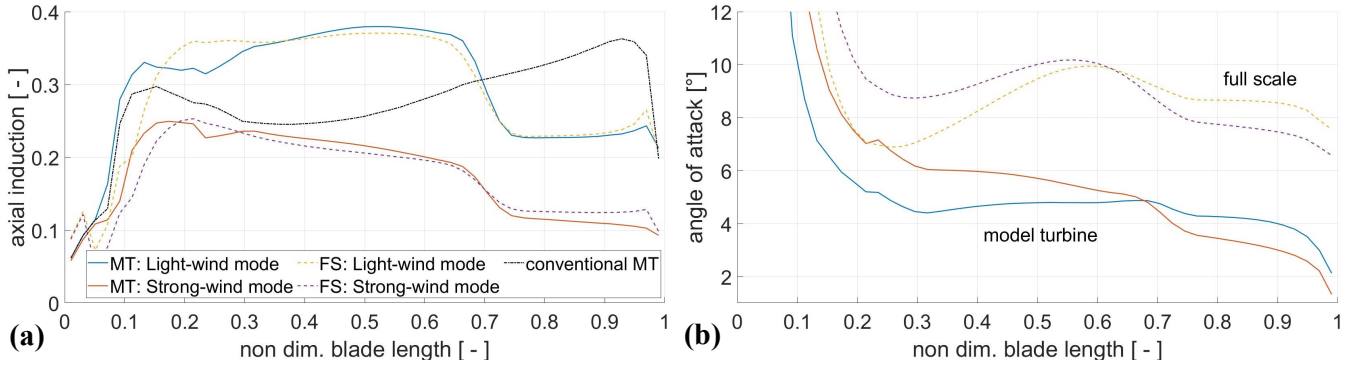
Figure 6. Axial induction (a) for light-wind mode (at u_ts) and strong-wind mode (at u_te) for the Hybrid-Lambda model turbine (MT), the full-scale rotor (FS) and the conventional model turbine in BEM simulations and respective angle of attack distributions (b).

Table 1. General parameter of the wind tunnel model and the full-scale Hybrid-Lambda Rotor

Parameter	Symbol	Model scale (subscript m)	Full-scale (subscript f)	Unit	Ratio
Length scaling factor	n_l			-	1/181
Time scaling factor	n_t			-	1/114
Rotor diameter	D	1.8	326	m	1/181
Max. rotor speed	ω_max	600	5.38	rpm	1/111
Rotor speed at u_ts	ω_trans	500	4.39	rpm	1/114
Design TSR inner 70 % of blade span	$\lambda_\text{d,SW}$	6	9	-	0.67
Design TSR outer 30 % of blade span	$\lambda_\text{d,LW}$	7.5	11	-	0.68
Wind speed, start of transition	u_ts	6.3	6.9	m s^{-1}	$0.93 \approx 114/(181 \cdot 0.68)$
Wind speed, end of transition	u_te	7.9	8.3	m s^{-1}	$0.95 \approx 114/(181 \cdot 0.67)$
Rated power	P_rated	340 *	$15 \cdot 10^6$	W	$0.74/181^2$
Reynolds number at 90% blade span at u_ts	Re	$95 \cdot 10^3$	$7 \cdot 10^6$	-	0.014

* reduced due to hardware constraints

3 Experimental and simulation methodology

In this chapter, we first explain the experimental set-up in Sect. 3.1, the measurement equipment in Sect. 3.2 and the post-
240   processing of the measurement data in Sect. 3.3. Several simulations are used to derive the blade design of the scaled model,
for comparison of the experimental data with simulation models and to get further insights into flow quantities that could not
be measured. The simulation methodology is therefore described in Sect. 3.4.

3.1   Experimental set-up
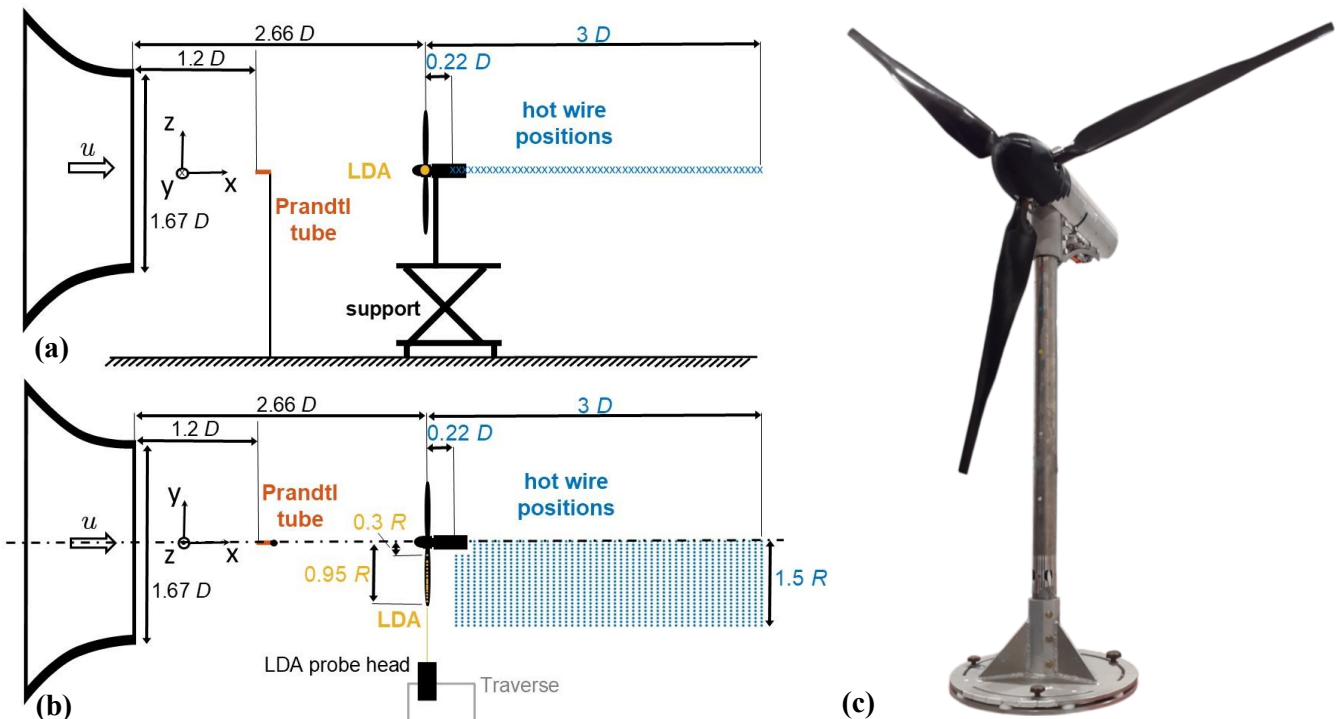
Figure 7. Experimental set-up, side (a) and top view (b), indicating the measurement positions of the hot wires, LDA and Prandtl tube. The
coordinate system is located in the rotor centre. MoWiTO 1.8 with the Hybrid-Lambda blades (c), $D = 1.8$ m, hub height of 1.5 m.

The experiments were carried out in the ~~turbulent~~ wind tunnel of Oldenburg, further described by Kröger et al. (2018). It is
245   a Göttingen-type wind tunnel, featuring a rectangular nozzle with a cross section of 3x3 m and a test section length of 30 m.
For the purpose of this study, the open jet test section configuration was used, as illustrated in Fig. 7. The wind tunnel can
be equipped with an active grid to realize turbulent, reproducible flow patterns in the inflow, as further explained by Neuhaus
et al. (2021). The active grid was mounted with static open flap configuration for the investigations of the rotor integrated
quantities (Sect. 4.1), the radially resolved measurements (Sect. 4.2) and for the wake measurements (Sect. 4.4). This leads to a
250   steady, uniform inflow over the rotor area with a turbulence intensity (T_i) of approximately 2%, which is used for all presented

measurements if not stated differently. Only for the wake investigations, four different levels of turbulence intensity (2%, 4%, 6% and 8%) were generated with the active grid. To analyse the effect of gusts on the rotor (see Sect. 4.3), the active gird was used to produce a transient wind speed change that is aimed to represent a scaled operating gust, as described by Neuhaus et al. (2021). According to the standard IEC 61400-1 (2019) the gust should last 10.5 s. With the time scaling ratio of 1:114

255 (as defined in Sect. 2) the ideally scaled gust in the wind tunnel would last only 0.09 s. Unfortunately, controlling the wind speed at such high frequencies is not possible and there is always a trade-off between high frequencies and sufficient wind speed amplitudes. Neuhaus et al. (2021) found the fastest gust with a reasonable gust amplitude with a duration of 0.75 s. This means, the gust in the wind tunnel is about 8 times slower than the respective full-scale equivalent. The amplitude reaches from $6.3\mathrm{m\,s}^{-1}$ to $7.5\mathrm{m\,s}^{-1}$ in the wind tunnel, while the IEC operating gust would range from $6.3\mathrm{m\,s}^{-1}$ to $8.2\mathrm{m\,s}^{-1}$.

260

In addition to the experiments with the Hybrid-Lambda Rotor, further measurements were carried out with the conventional blades to compare the load response due to gust events (see Sect. 4.3) and to compare the wake of the two blade designs (see Sect. 4.4). Both model rotors have the same rotor diameter of 1.8 m. The model turbine, as depicted in Fig. 7, is equipped with strain gauges in the blade root to measure the flapwise blade root bending moment and in the tower base to derive the rotor

265 thrust. A torque meter and a rotational encoder in the drive-train allow for measurements of the rotor torque, azimuthal position and rotational speed. The data acquisition system of the model turbine samples the aforementioned measurement data with 5 kHz. The blade pitch is set by three DC motors, mounted in the individual blade roots, allowing for individual pitch control. However, in this analysis, only collective pitch settings are used.

270 For this study, the turbine is operated at a fixed rotational speed of 500 rotations per minute (rpm). Changing the rotational speed would influence the operational Reynolds number which effects the aerodynamic behaviour of the turbine. For the sake of comparability between all conducted measurement runs, a fixed reference rotational speed is chosen. Also for the gust investigations, the rotational speed and the pitch is set to constant values. Since the focus of this study is on the aerodynamic behaviour and the impact from the different blade designs, no overshadowing of the effects by controller actions is desired.

275

The model turbine is placed 4.8 m (2.66 D) behind the wind tunnel nozzle and the inflow velocity is measured with a Prandtl tube and a pressure transducer 2.1 m (1.2 D) behind the nozzle. These values were found to be best practice in order to avoid influences of the induction zone of the model turbine on the wind speed measurements and on the development of the inflow behind the active grid.

280

3.2 Measurement equipment and experimental matrix

To measure the axial and tangential induction a 2-dimensional Laser-Doppler-Anemometer (LDA) with a power of 1 W for each laser is used. A beam expander with a focus length of 2.1 m allows to mount the LDA system in a reasonable distance in order not to disturb the flow. In the radial direction, 16 measurement points are taken on the 3 o'clock position (looking

285 downstream) in order to minimize the tower effects on the measurements (rotor is spinning clockwise looking downstream). The measurement points cover a range from 0.3 R to 0.95 R with a closer spacing in the region of the expected steep induction gradients, as indicated in Fig. 7. The axial and tangential induction and ~~further~~ the angle of attack are derived from ~~a~~ method introduced by Herráez et al. (2018) and further applied by Berger et al. (2021). Here, the axial and tangential velocity components are probed in the bisectrix of two blades where the local blade induction is counterbalanced and cancelled out. Herráez

290 et al. (2018) found that the trailed vorticity at the blade tip does play a non-negligible role and measurements further outboard than 0.92 R should be treated with care. This method is only valid for axial and uniform inflow which is given for the studies presented here.

We analysed the wake of both the conventional and the Hybrid-Lambda Rotor. The light-wind mode of the Hybrid-Lambda

295 Rotor leads to a thrust coefficient of 0.92. The conventional blades are investigated at the same wind speed with the same ~~rpm~~ and the pitch is set in order to achieve the same thrust coefficient as for the Hybrid-Lambda blades in light-wind mode. Further, the thrust coefficient is 0.61 for the strong-wind mode and 0.45 for rated wind speed. The investigated operating modes are summarized in Table 2. Hot-wire measurements were performed downstream of the rotors at hub height on a horizontal line along the 3 o'clock position. A hot-wire rig with 24 one-dimensional hot-wires was used, covering a radial range from

300 the centre of rotation to 1.38 m (0.77 D) with an equidistant spacing of 6 cm (0.033 D). The hot-wire rig was mounted on a traverse to realize a very fine spacing in the downstream direction, too. Measurements are taken at 51 positions downstream from the rotor, from 0.4 m to 5.4 m (0.22 D to 3 D) with a spacing of 0.1 m (0.056 D). The first three downstream positions are located next to the nacelle. Overall, this leads to a very high spacial resolution of the wake measurements, resulting in an equidistant grid of 24 x 51 measurement points covering a rectangle of 1.38 x 5.4 m which is illustrated in Fig. 7. The hot-wire

305 measurements are sampled with 6 kHz over a duration of 40 s for each point. Only for the investigation of varying inflow turbulence intensities, a different hot-wire rig was used. In this case, the hot-wires were mounted with a spacing of 4 cm with 16 hot-wires ranging from 0.35 D to 0.68 D and only the downstream position of 0.4 D was investigated.

Table 2. Investigated operating modes for the Hybrid-Lambda wind tunnel model

	Light-wind mode	Strong-wind mode	Rated	Unit
Abbreviation	LW	SW	rated	-
Wind speed	$u_{ts} = 6.3$	$u_{te} = 7.9$	$u_{rated} = 9.4$	m s^{-1}
Rotor speed	500	500	600	rpm
TSR	7.5	6	6	-
Pitch angle	-0.8	3.2	6.7	°
c_T experiment	0.92	0.61	0.45	-
c_P experiment	0.42	0.35	0.27	-

To characterize the scaled Hybrid-Lambda Rotor and to derive the rotor integrated quantities, a measurement matrix was
310 performed, consisting of a grid of TSR and pitch combinations with the turbine operating at steady-state conditions. This matrix covers TSRs from 5 to 9 with a spacing of 0.5 and pitch angles from $-2°$ to $+4°$ with a spacing of $1°$. Further, a finer grid is applied in the area of highest interest around the maximum power coefficient. From $-1.6°$ to $-0.4°$, the pitch angle is varied in steps of $0.4°$ and the TSR is varied from 6.75 to 8.5 in steps of 0.25. The combination of very low TSR and pitch values could not be measured since the structural loads would exceed the safety constraints of the model turbine. However, according
315 to the Hybrid-Lambda control strategy, the pitch angle is increased when the TSR is lowered. Consequently, the combination of low TSR and low pitch values is unlikely to be relevant. In total, 91 points were measured. For each point, the turbine data is averaged over 15 s which corresponds to 125 rotor revolutions. The non-dimensional power and thrust coefficients c_p and c_T are calculated with the inflow wind speed derived from the Prandtl tube measurements and the density calculated from air temperature, humidity and ambient pressure. Since all measurements for the rotor integrated quantities are recorded within one
320 day, the maximum variation in the air density was only 0.2% and the air density is considered error-free in the error propagation. For the power and thrust coefficients, the error-prone variables are thrust force, rotor torque, inflow velocity and rotational speed.

3.3 Measurement data post-processing and uncertainty estimation

325 Certain correction methods are applied to the turbine load measurements, as described in the appendix of (Berger, 2022). The measured torque is corrected for the drive train friction, resulting from the bearings and the slip ring in order to derive the rotor aerodynamic torque. The friction was derived as a linear function of rotational speed from calibration measurements, where the drive train is rotated without the blades. The thrust is corrected for the aerodynamic drag on the tower and nacelle. The drag force was derived by wind tunnel measurements with detached blades resulting in a quadratic correction function of the
330 thrust force over the wind speed. When calculating the wind speed at the location of the tower, induction effects are taken into account, within an iterative process according to the momentum theory, as further described by Berger (2022). The strain gauge measurements are post-processed with a zero-phase digital filter, using a Butterworth infinite impulse response low-pass filter with a half-power-frequency of 28 Hz which is 12% higher than the blade passing frequency (3P). This ensures that all relevant rotor dynamics are resolved, but allows to filter the data for high frequency vibrations and noise.

335

The LDA measurement data is post-processed as follows. First, the data is synchronized with the azimuth angle measurements of the MoWiTO 1.8. From the continuously acquired LDA data, only the values that lay in a sector of $+/-3°$ from the blade bisectrix are further considered. For each radial position, the data is recorded for 60 s which corresponds to 1500 blade passings. The LDA data is not recorded in equidistant time steps, but whenever a seeding particle passes through the
340 probe volume. Due to the nature of the flow, more samples will be available for the axial component compared to the tangential component. On average, 17000 samples were used for the calculation of the mean value of the tangential velocity and 37500 samples for the axial velocity, for every radial position. The number of samples was never lower than 14700 and 29000 for the

tangential and axial velocity component, respectively. Therefore, the confidence in the mean value is very high and the 95%
confidence interval would not be visible in the plots. Consequently, we decided to plot the standard deviation over all samples
345 which visualizes the spread of the data, but does not represent the high confidence in the mean value. In order to calculate
the axial induction, precise information about the inflow is needed. Therefore, the inflow is measured with the LDA along a
horizontal line at hub height in the position of the rotor plane with the turbine not installed. These measurements result in an
observation of the mean wind speed and the respective standard deviation for all positions where the axial induction should be
calculated. The inflow characterization reveals a slight drop of the axial inflow velocity from the centre to the edge of the rotor
350 area of $0.25\ m\ s^{-1}$. This marginal non-uniformity is accounted for in the calculations of the axial and tangential induction and
of the angle of attack, since the information of the inflow at the individual radial position is used, as indicated in Eq. 10 to 12.
Here, a and a' are the axial and tangential induction factors, u_{ax} and u_{ta} are the axial and tangential velocity components in the
rotor plane, u_{∞} is the undisturbed axial inflow velocity component in the rotor plane, r is the radial position, ω is the rotational
speed, α is the angle of attack and γ is the geometrical angle between the chord of the local blade segment and the rotor plane,
355 consisting of twist and pitch.

$$a(r) = 1 - \frac{u_{\mathrm{ax}}(r)}{u_{\infty}(r)} \tag{10}$$

$$a'(r) = \frac{u_{\mathrm{ta}}(r)}{\omega r} \tag{11}$$

360 $$\alpha(r) = \arctan\left(\frac{u_{\mathrm{ax}}(r)}{u_{\mathrm{ta}}(r) + \omega r}\right) - \gamma \tag{12}$$

Measurement uncertainties are calculated with the Gaussian error propagation and if not stated differently, error-bars indicate
the combined standard deviation of all measurement uncertainties, as indicated in Eq. 13. Here, ∂ refers to the partial deriva-
tive of the respective equation, $f(x_i)$ is the combined measurement value which is calculated from n multiple measurement
variables x_i and σ is the standard deviation of the respective variable. Unless indicated differently, the latter is derived directly
365 from the measurement data. We assume, $\sigma(r) = 2\ mm$ and $\sigma(\gamma) = 0.2°$.

$$\sigma(f(x_i)) = \sqrt{\sum_{i=1}^{n}\left(\frac{\partial f}{\partial x_i} \cdot \sigma(x_i)\right)^2} \tag{13}$$

For the investigation of the gust events in Sect. 4.3, ensemble averaging is performed. The gust event is repeated 45 times
with the active grid which is synchronized with the turbine's data acquisition system. The measurement data of the resulting
flapwise blade root bending moment is aligned for all repetitions and an average value and the standard deviation at each
370 time step of the gust are constructed. This approach can smooth out non-deterministic variations. The same transient inflow
conditions were applied to the conventional blades as well as to the scaled Hybrid-Lambda Rotor. In this case, we use the 95%
confidence interval of the 45 repetitions, to indicate the statistical significance of the different behaviours of the two blade sets.

For the sake of comparability, we normalized the RBM measurements with the mean stationary value of the respective blade set. Nevertheless, the difference between the two blade sets in the mean stationary value was only 0.2 Nm which corresponds
375 to 3% of the mean value.

3.4 Simulations

The scaled version of the Hybrid-Lambda Rotor was designed with an in-house BEM code, as described in Hansen (2008). The radially resolved axial induction and angle of attack distribution was derived with this simulation tool. In this paper, we define
380 the axial induction as averaged over the annulus which can be expressed as the local axial induction on the blade multiplied by the tip-loss factor. Additionally, aero-elastic simulations were carried out with OpenFAST V3.1 (Jonkman et al., 2022) for model validation. The rotor integrated quantities (c_p, c_T and flapwise RBM) shown in this study are derived from the Open-FAST simulations. The two above mentioned tools ~~both~~ implement the Prandtl tip and root loss models and the Glauert high thrust correction with the approximation by Buhl (2005). Neither of them uses a dynamic stall or dynamic inflow model, since
385 the reference simulations in this study are restricted to steady and uniform inflow. The tower shadow effect is modelled only in OpenFAST. In preliminary analyses, the blade tip deflection in front of the tower was measured with a laser distance sensor and it did not exceed 15 mm in steady-state operations. However, the blades are modelled flexible in OpenFAST using ElastoDyn as the elastic solver (Jonkman and Sprague, 2021). The tower is modelled rigid for both tools. Since the in-house BEM code is purely aerodynamic, all components are modelled rigid in this case.
390

For additional investigations on the radial flow component in the rotor plane (Sect. 4.2) and the wake behaviour of the Hybrid-Lambda model rotor and the conventional model rotor (Sect. 4.4), FVW simulations are carried out with the module OLAF in OpenFAST V3.5, as described by Branlard et al. (2022) and Shaler et al. (2020). No tower shadow model is used and the core spread eddy viscosity (viscous diffusion parameter) is set to 100, as we aimed for a representation of an undisturbed
395 wake, focusing on the effects that result from the aerodynamic blade design. Further, no nacelle drag model is implemented in OLAF, at the time of this study. For all simulations, the inflow is modelled as uniform over the rotor area and constant in time without added turbulence. Similar as to the experiments, the comparison of the Hybrid-Lambda Rotor and the conventional rotor is carried out at the same thrust coefficient in light-wind mode.

4 Results

400 In this section the results from the wind tunnel experiments and the complementary simulations are presented. We first address rotor integrated quantities in Sect. 4.1 and then expand to radially resolved measurements in Sect. 4.2. Next, we compare the dynamic response of the Hybrid-Lambda Rotor due to gusts with the response of the conventional rotor in Sect. 4.3. Finally, we characterize and compare the wake of the two model wind turbines in Sect. 4.4.

4.1 Rotor integrated quantities

405 ~~Characterizing the newly designed model rotor is an important step.~~ The ~~derived~~ performance curves of power coefficient, thrust coefficient and flapwise RBM, resolved over a fine mesh of TSR and pitch, are used to validate the blade design and to define operating points for further experiments. Such a characterization is further needed for controller implementations in future studies. In total, 91 combinations of TSRs and pitch angles were measured with a constant rotational speed of 500 rpm. For the sake of clarity, only a small portion of the results is plotted in Fig. 8. Overall, the measured power coefficient shows good

410 agreement to the BEM simulations. The measurement values are lower than those from the ~~reference~~ simulations which could indicate that the simulated airfoil polars overestimated the performance at the low Reynolds numbers. Both, measurements and simulations show the highest power coefficient at similar operating points, i.e. TSR and pitch combinations. The difference in maximum c_{p} between measurement and simulation data is about 2%. Differences are larger for off-design operational points, such as the combinations of large pitch angles with very high or very low TSRs. The curves of the thrust coefficient show a

415 similar shape over TSR and pitch angle, compared to the simulations but with a considerable offset. For the operating point with maximal c_{p}, an offset in the thrust coefficient of about 13% is present. The non-dimensional flapwise RBM is plotted in Fig. 8 and is defined in Eq. 14.

$$c_{\mathrm{RBM}} = \frac{M_y}{0.5\rho u_\infty^2 R \frac{\pi R^2}{3}} \tag{14}$$

Here, $0.5\rho u_\infty^2$ is the dynamic pressure, R is the rotor radius used as a characteristic length and $\frac{\pi R^2}{3}$ is the rotor area devided

420 by the number of blades. The measured flapwise RBM are in good agreement with the simulations. The relative difference of the measured RBM and the simulations is 4% in the operational point of maximum c_{p}.
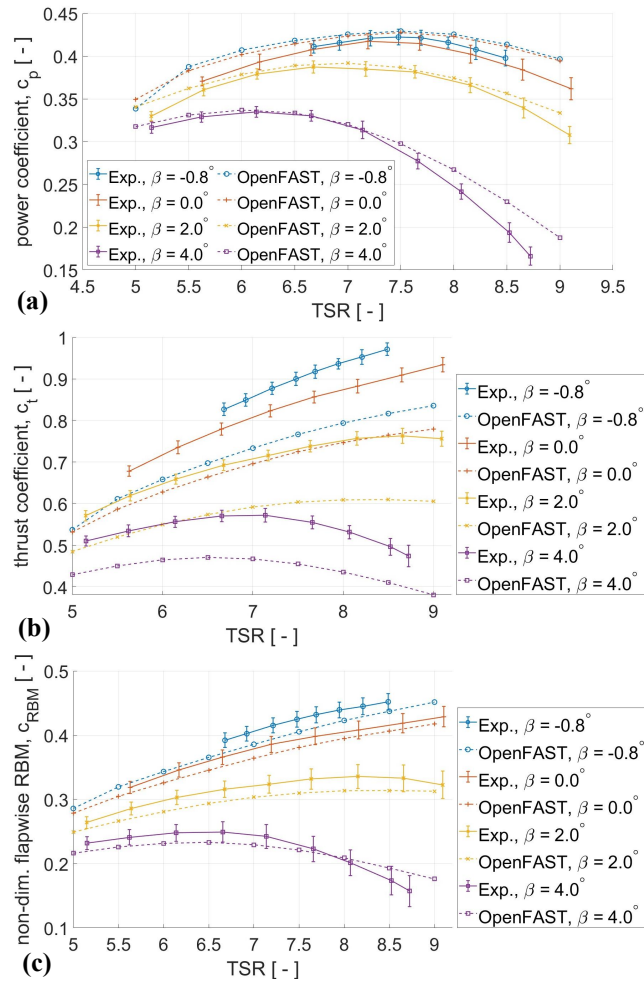
Figure 8. Power coefficient (a), thrust coefficient (b) and non-dimensional flapwise RBM (c) from measurements and BEM simulations for various TSR and pitch angles β, at constant rotor speed of 500 rpm.

4.2 Radially resolved quantities

In this section, we address the measurements of axial induction and angle of attack distribution over the blade span. We further investigate the radial velocity component in the rotor plane, as derived from FVW simulations, since this quantity was not mea-

425   sured within the ~~given~~ measurement campaign. The measurements of the axial induction with the LDA show a fair match with the BEM simulations for the inner blade region ($r/R < 0.7$) for both operating modes, as displayed in Fig. 9. However, the steep gradients in the blending region of the blade design are not ~~captured by~~ the LDA measurements. The measurements show a smeared out and less steep gradient at $r/R \approx 0.75$. Further, the two outermost measurement points should be treated with care since the tip loss effect influences the bisectrix method by Herráez et al. (2018). The derived angle of attack distributions

430   are plotted in Fig. 9. The measurements show that ~~the contrary tilting of the distribution works, i.e.~~ when switching from the

light-wind to the strong-wind mode, the angle of attack increases for the inner 70% of the blade length and decreases for the outer 30%. Overall, a minor offset of about $0.6°$ between the measurements and the simulations can be observed. However, the slopes of the angle of attack distribution match reasonably well, with the exception to the tip region where the tip loss effects play a non-negligible role.

435
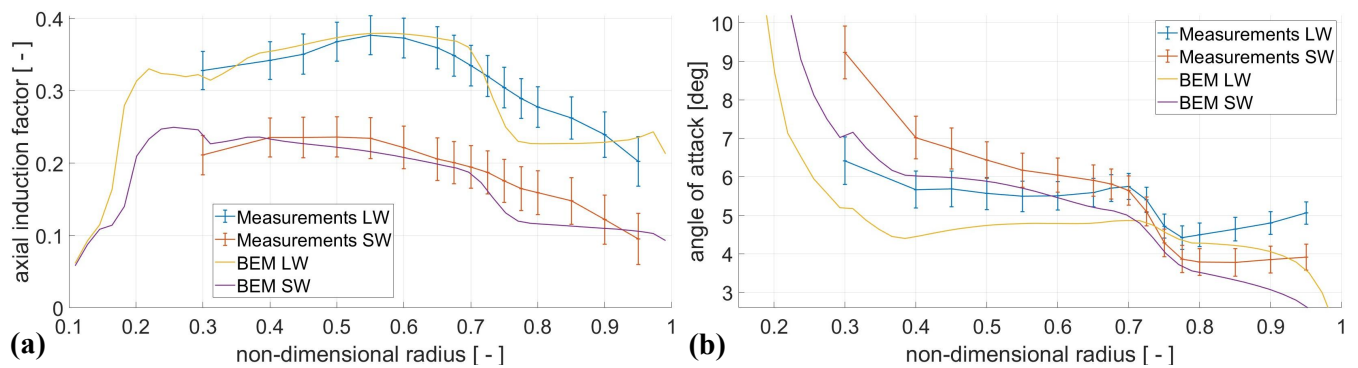
Figure 9. Axial induction along the blade span (a) and Angle of attack (b) from measurements and BEM simulations for the light-wind (LW) and strong-wind (SW) mode

Next, we ~~want to~~ explore possible reasons for the ~~smeared out~~ gradients in the axial induction distribution. In the BEM theory, the blade elements are treated independent of each other. This assumption is clearly violated with the ~~given~~ blade design of the Hybrid-Lambda Rotor. To reveal further insights in the flow in the rotor plane, we use FVW simulations for the conventional and the Hybrid-Lambda model turbine. The radial velocity component is extracted on a horizontal line in the rotor plane

440 in a non-rotating coordinate system and the average over all time steps is shown in Fig. 10. The used time step corresponds to an azimuthal resolution of $1.5°$. Figure 10 shows the envelope, i.e. the minimum and maximum of the radial flow, thus displaying the impact of the passing blades and the associated vortices. A comparison of the two blade designs confirms an increased radial outboards flow component for the Hybrid-Lambda Rotor, almost over the entire rotor span. But, it is especially increased in the ~~design~~ blending region ~~of~~ 70% blade length. The envelope shows lower extreme values at the blade tip for

445 the Hybrid-Lambda Rotor. This is due to the increased axial wind speed component in the outer rotor annulus. Consequently, the difference in wind speed to the free stream is lower and less radial flow is observed. The conventional rotor has a much higher axial induction near the blade tip (compare with Fig. 6) which explains the larger magnitudes in the radial flow envelope. But, the envelope also reveals a second peak in the blending region of the Hybrid-Lambda Rotor which means that the shear layer between the axial flow in the inner rotor disk and the outer annulus also introduces additional radial flow. This clearly

450 highlights that the blade elements can not be treated independently and complex, three-dimensional flow structures lead to the smearing of the steep gradients. Figure 10 also shows the differences in the radial flow between the operating modes. When the Hybrid-Lambda Rotor switches from light-wind to strong-wind mode, the radial velocity component decreases because the axial induction and the thrust coefficient are reduced and there is less widening of the stream tubes. In contrast, the conven-

tional rotor maintains the same operational point (same TSR and pitch angle) until rated wind speed, since no load limitation is

455   applied. This means, the thrust coefficient and the axial induction remain constant. When the axial wind speed increases, also the radial velocity component will increase in the rotor area of the conventional turbine, as absolute velocity values are plotted in Fig. 10. The flow in the wake of the Hybrid-Lambda Rotor is further investigated in Sect. 4.4 and the influence of the trailing vortices is explained, which also heavily influence the flow in the rotor area.
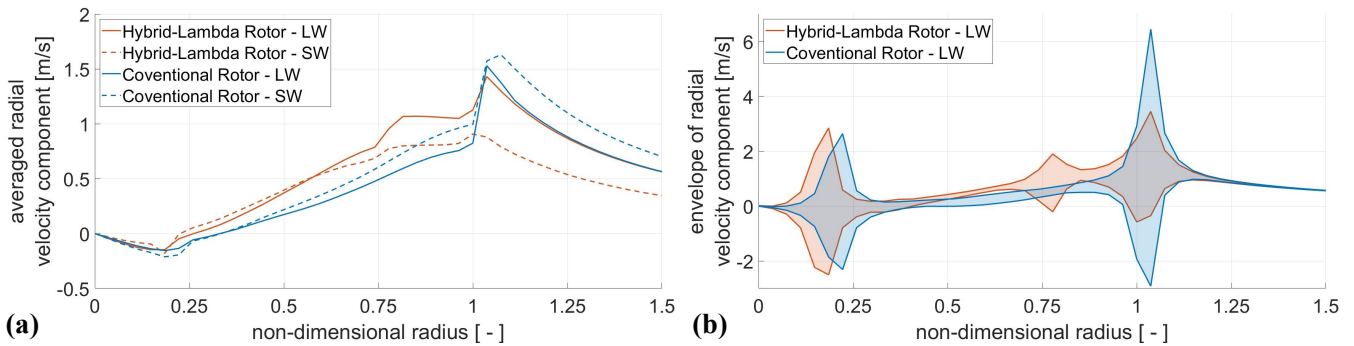
Figure 10. Averaged radial velocity component (a) and envelope of the radial velocity component (b) in the rotor plane from FVW simulations for the two model turbines

460   From the FVW simulations we can further extract the stream lines for both model turbines which are shown in Fig. 11. The streamlines that pass along the tip of the rotors are almost identical among the two turbines. This means, the outer shape of the wake is similar. In contrast, the streamlines of the Hybrid-Lambda Rotor inside the wake are pushed further outwards, compared to the conventional model turbine. Here, the effect of the increased radial flow is visible. If one considers the conservation of mass flow, the slower air in the inner part of the rotor has to expand into the outer wake annulus (compare with the wake

465   investigations in Sect. 4.4). Thus, the streamlines in the outer part of the wake are closer together.
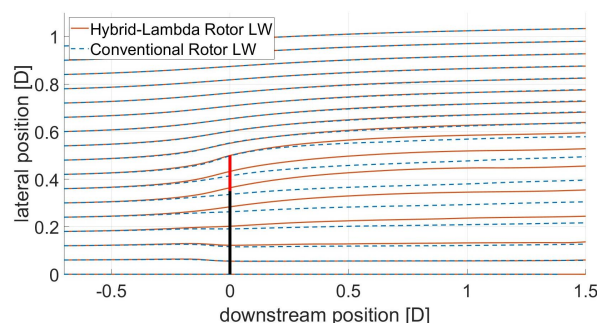
Figure 11. Streamlines from FVW simulations for the Hybrid-Lambda model turbine in LW mode and the conventional model turbine (same c_T). The rotor is indicated with the vertical black bar, the low-induction tips are displayed in bright red.

4.3 Dynamic response to gust events

We compared the response of the flapwise RBM to gust events among the two sets of blades. The gust events were generated with the active grid, mimicking a scaled extreme operating gust wth the so-called Mexican hat shape, according to IEC 61400-1 (2019). The inflow was characterized by Neuhaus et al. (2021) with hot-wire measurements of multiple repetitions in the centre

470 of the rotor plane which are plotted in Fig. 12. ~~This setting was derived as~~ the optimum trade-of between the frequency and the amplitude of the gust, as described in Sect. 3.1. The oscillations in the wind speed after the gust event (for $t > 3.2 \ s$) are a pumping-effect of the flow induced by the active-grid which can not be avoided for such fast changes in the wind speed. The ensemble averaged response in the flapwise RBM for the two rotors is displayed in Fig. 12. Note, that no wind turbine controller was applied in this study. The pitch angle remains constant and the rotational speed is controlled to be constant over

475 the entire gust event. The Hybrid-Lambda Rotor is in light-wind operating mode during the steady inflow period before the gust event. The conventional rotor is operated at the same TSR of 7.5 and the pitch is set in order to match the same flapwise RBM among the two rotors in the steady inflow period. This allows us to compare the pure aerodynamic response of the rotors. The amplitude of the load overshoot is less for the Hybrid-Lambda Rotor and the maximum flapwise RBM is 4.3% higher for the conventional blades. The reduced axial induction in the outer part of the Hybrid-Lambda blades helps to mitigate the load

480 overshoot. Similar conclusions were drawn by Ribnitzky et al. (2024) when comparing the effect of extreme wind shear events on the 15 MW Hybrid-Lambda Rotor and a reference rotor on a full-scale level with BEM simulations.
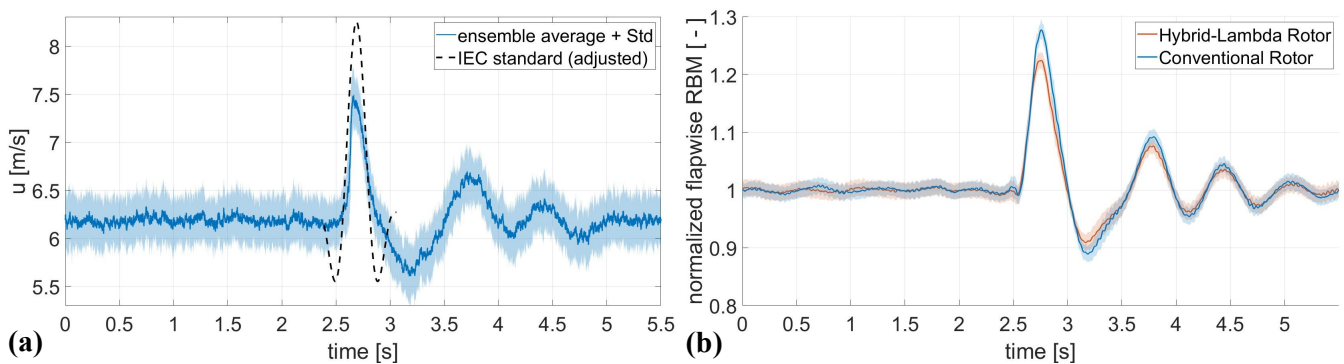
Figure 12. Left: Gust in the wind tunnel: Inflow hot-wire measurements in the rotor plane and scaled IEC gust, displayed 8 times slower than ideal scaling, gust amplitude is not scaled (a). Right: Flapwise RBM response of the Hybrid-Lambda and the conventional rotor. The shaded area indicates the 95% confidence interval of the 45 repetitions of the gust event (b).

4.4 Wake characterization

In this section, we provide an in-depth analysis and comparison of the wake of the two rotors, using hot-wire measurements and FVW simulations. The hot-wire measurements are performed in the open jet configuration of the wind tunnel, as explained

485 in Sect. 3.1. For large distances to the wind tunnel nozzle, there is an unavoidable interaction of the wind tunnel shear layer

with the wake of the turbine. Measurement data for downstream distances larger than 2 D should be treated with care, especially for larger lateral distances to the centre line. Nevertheless, the data can provide an impression of the big picture and we consequently decided to plot the data up to 3 D downstream. Figure 13 shows the normalized wind speed and the turbulence intensity in the wake of the two rotors. A major advantage of the Hybrid-Lambda Rotor becomes clear when comparing the

490 wake for the different operating modes. When the wind speed increases and the rotor shifts to strong-wind mode and further to rated conditions, the wake deficits are greatly decreased (see also Fig. 14) and the opening angle of the wake (e.g. the expansion of the stream tube) is reduced. This is of immense importance when evaluating the rotor concept in wind farm applications. In contrast, a conventional rotor would operate with the same axial induction and thrust coefficient until rated wind speed. Consequently, the wake deficits remain unchanged and we only provide one plot for the conventional rotor. The second aspect

495 that we discuss is the shape of the wake. The axial induction distribution of the Hybrid-Lambda Rotor is clearly mirrored in the wake profiles. The low-induction design of the outer 30% of the blades leads to an outer annulus with reduced wake deficits. In contrast, the inner part of the blade is designed for a higher axial induction compared to the conventional rotor (see Fig. 6), thus resulting in lower wind speeds in the centre of the wake. Note, that the axial induction is a free design variable in the Hybrid-Lambda design methodology and the blade design could be adjusted when optimizing for the mitigation of wake effects, e.g.

500 choosing a slightly lower axial induction for the inner blade section. However, the wind tunnel model of the Hybrid-Lambda Rotor was not designed to outperform the conventional model in terms of wake effects, but with the objective of incorporating the wake characteristics of the full-scale Hybrid-Lambda model.

The outer annulus with reduced wake deficits leads to a second shear layer at the boarder to the inner wake core with lower

505 wind speeds. This is also seen in the local turbulence intensity in Fig. 13, which is defined as $T_{\mathrm{i}} = \sigma(u(x,y))/u_{\mathrm{mean}}(x,y)$. For now, we only address this as a shear layer, since the vorticity can not be derived from one-dimensional hot-wire measurements. We further look into the vorticity in the following paragraphs. The conventional rotor exhibits one single shear layer between the wake and the free-stream which leads to a single ring of increased turbulence intensity that widens up with further downstream distances. In contrast, for the Hybrid-Lambda Rotor, two rings of increased turbulence intensity can be observed.

510 However, the magnitude of the turbulence intensity of both rings is lower compared to the single ring from the conventional rotor. The first ring emerges from the blade tip, the second one is shed at the blending region on the blade at 70% blade length (if one considers the opening angle of the wake). Travelling downstream, these two shear layers widen up and start to interact with each other which finally leads to a region of ~~very~~ high turbulence intensity for downstream distances larger than 2 D. This effect is most prominent in the light-wind mode. However, the two rings of increased turbulence intensity are still noticeable

515 in the strong-wind mode and at rated conditions. Figure 13 further shows how the shape of these rings change among the operating modes. While they are bent outwards in the light-wind mode, the curvature and opening angle decreases when switching to strong-wind mode and the rings are almost straight. At rated conditions, they even tend to have a slight inwards directed taper.

From previous FVW and LES simulations on the full-scale Hybrid-Lambda Rotor, Ribnitzky et al. (2023) discovered that

520 with increasing turbulence intensity in the inflow, the outer annulus with reduced wake deficits smears out. This means, the
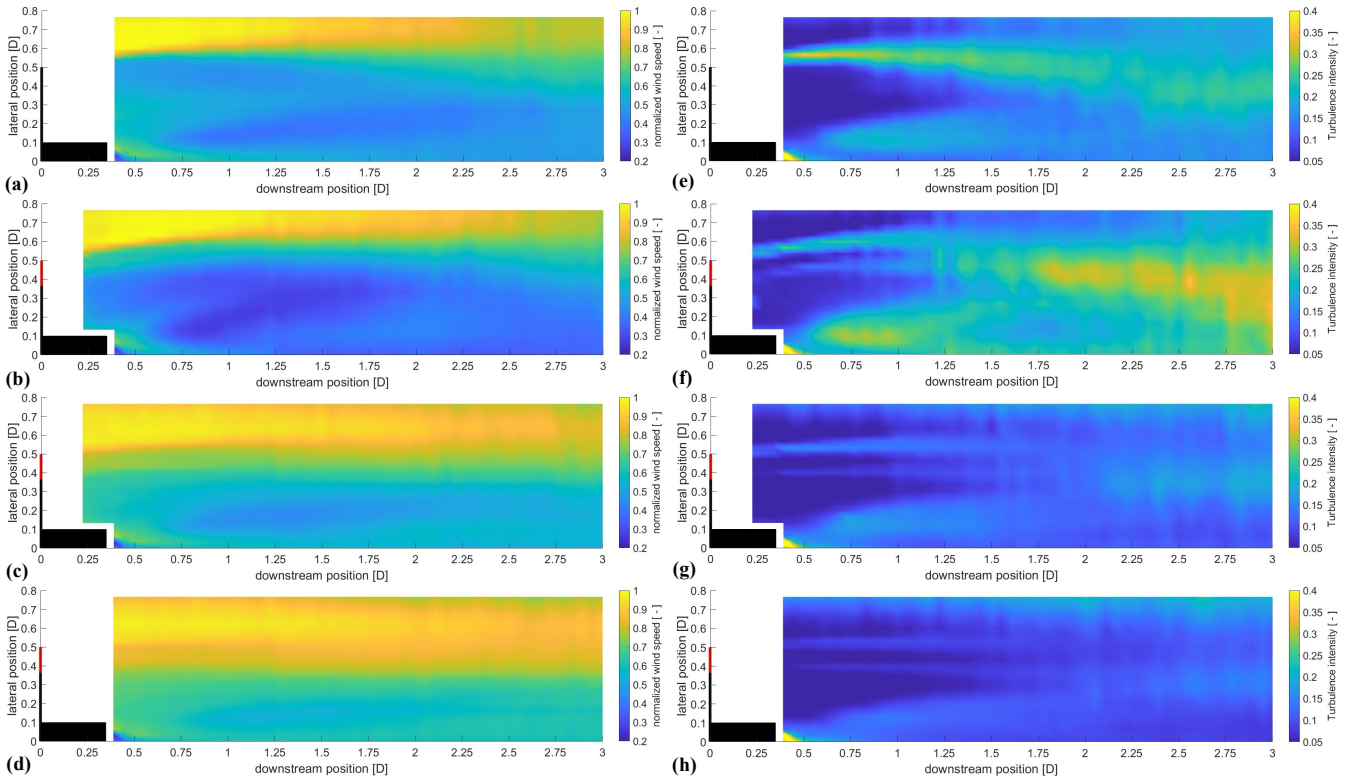
Figure 13. Mean normalized wind speed (a-d) and turbulence intensity (e-h) from hot-wire measurements in the wake of the model turbines. From top to bottom: Conventional rotor (a,e), Hybrid-Lambda Rotor in LW mode (b,f), SW mode (c,g) and at rated wind speed (d,h). Nacelle and blades are displayed in black, the outer 30% of the Hybrid-Lambda blades are displayed in red.

step-shaped wake profile with a region of constant high wind speed in the outer annulus develops more in to a gradual change between the inner and outer wake deficit. This transition happens closer to the rotor for higher turbulence levels. To further investigate this, hot-wire measurements were performed 0.4 D behind the rotor with a hot-wire spacing of 4 cm (instead of 6 cm for all other cases presented before) with four different turbulence intensities in the inflow, generated with the active-grid.

525 The free-stream velocity among the different turbulence-levels was not exactly matched, since the activation of the active grid impacts the mean wind speed. Although the active gird protocols were iterated in order to match the free-stream velocity as best as possible, small deviations of around 5 to 10 % in the free-stream velocity remain. However this does not affect the gradients of the wake profiles which is the focus of interest in this case. The results are shown in Fig. 14 and the smearing of the outer wake annulus is clearly visible. Especially for the case with 8% inflow turbulence intensity, the plateau with higher

530 wind speeds vanishes.

~~The assumption is obvious that~~ the inner shear layer is also coupled to an additional vortex system that emerges from the blending region on the blade. Since the vorticity can not be derived from one-dimensional hot-wire measurements, we use
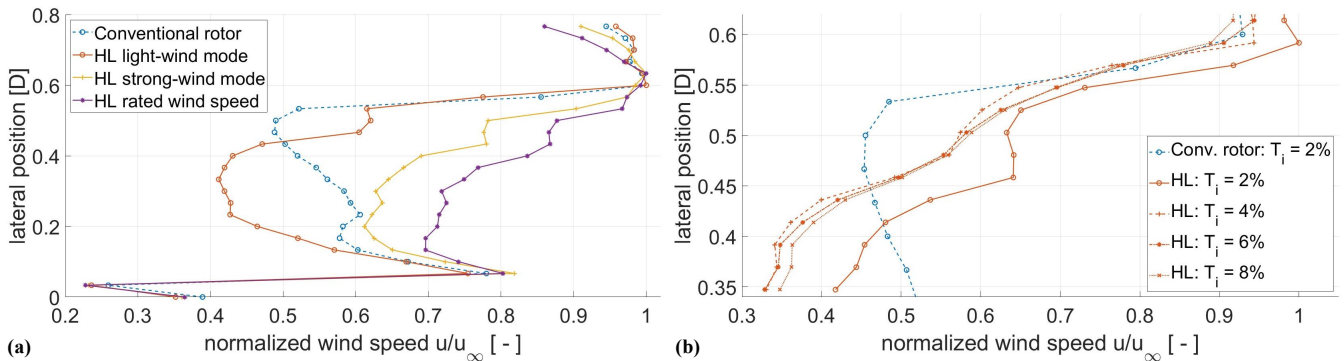
Figure 14. Wake profiles at 0.4 D downstream distance for the two model rotors. Left: At $T_i = 2\%$ for different operating modes (a). Right: In light-wind mode for different T_i (b).

FVW simulations to investigate this assumption. First, the FVW simulations confirm the characteristics of the wake of the Hybrid-Lambda Rotor. The mean wind speed, plotted in Fig. 15, also shows the outer annulus with higher wind speeds in both operating modes and the reduced wake deficits and the reduced wake expansion in the strong-wind mode. The vorticity is computed as the magnitude of the three vorticity-components. The vorticity plots clearly highlight a second ring of vortices emerging from the blending region on the blade. The magnitude of the vorticity is lower than for the tip vortex as also observed in the turbulence intensity derived from the hot-wire measurements. The FVW simulations are set up in a way to produce a wake that is as undisturbed as possible, e.g. using laminar and uniform inflow and a relatively low core spread eddy viscosity. Consequently, the vortex systems do not break up noticeably and the interaction between the inner and outer ring of vortices is rather low.

All in all, the measurement results are in very good agreement to the FVW and LES simulations that were carried out by Ribnitzky et al. (2023) on the 15 MW full-scale Hybrid-Lambda Rotor, where also an improved wake recovery was observed. In short, the results indicate three major advantages of the Hybrid-Lambda Rotor in wind farm applications. First, the decreased wake deficits for a large range of wind speeds below rated (for $u_{ts} < u < u_{rated}$), the increased wind speeds in the outer wake annulus which is beneficial for partial wake scenarios, and the enhanced wake mixing due to the additional shear layer and vortex system in the wake.
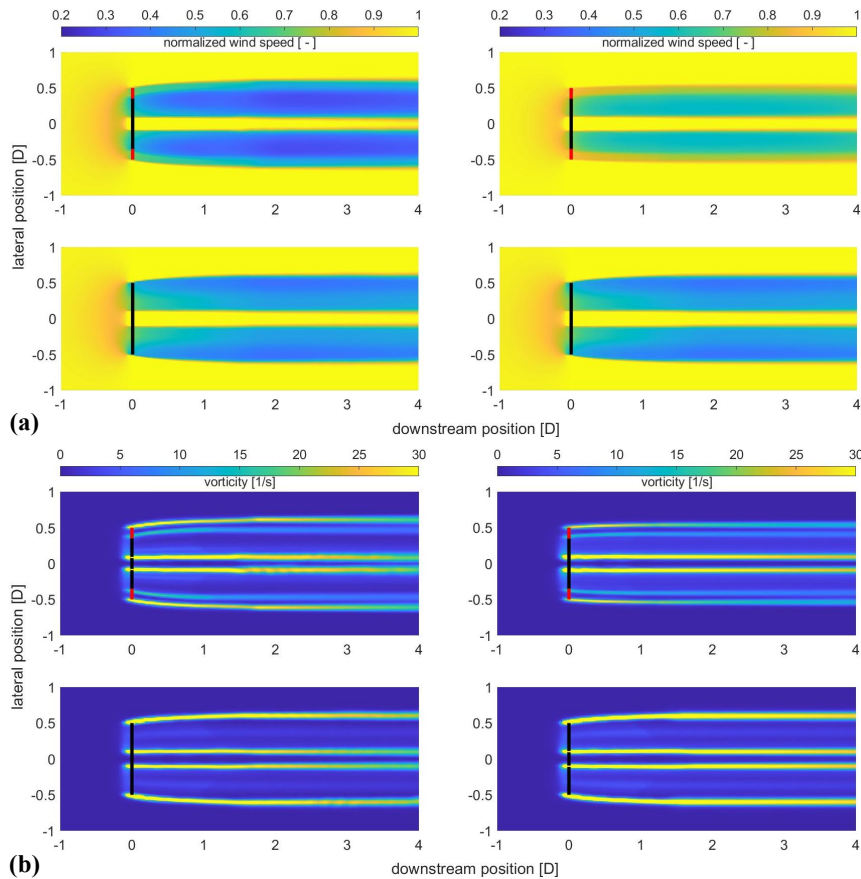
Figure 15. Normalized wind speed (a) in light-wind (left) and strong-wind mode (right). Vorticity magnitude (b) in light-wind (left) and strong-wind mode (right), for the Hybrid-Lambda model turbine (top) and the conventional model turbine (bottom) from FVW simulations

5   Discussion

Scaling wind turbine rotors to wind tunnel size is a delicate scientific task since not all physical characteristics can be matched exactly. The scaling objectives need to be defined precisely and compromises need to be made regarding the matching of classical aerodynamic non-dimensional parameters. In this paper, we developed a method on how to scale the Hybrid-Lambda Rotor to wind tunnel size with objectives that differ from other aerodynamic scaling approaches found in the literature, as described among others by Canet et al. (2021), Bottasso and Campagnolo (2021) and Gasch and Twele (2012). The concept involves a blade design for two TSRs which is a challenge on its own. But additionally, we need to transfer the design method to lower TSRs in order to derive ~~large enough~~ chord lengths and Reynolds numbers. This leads to a novel scaling approach, coupled with the objective of matching the non-uniform distribution of axial induction along the blade span for two different operating modes.

This scaling approach fulfilled its aim in replicating the aerodynamic characteristics ~~on the~~ wind tunnel scale by ~~the~~ means of an aerodynamic redesign with low-Reynolds number profiles. For the sake of comparability with the reference model turbine, as described in Berger et al. (2018), we choose the same airfoils, SG6040 and SG6041. Although we decided differently, we want to pinpoint future designers of model wind turbines to the low-Reynolds number airfoil SD7032, which was experimen-
565 tally investigated by Fontanella et al. (2021) and a high quality data set for the airfoil polars under various Reynolds numbers is available.

The investigation of the scaled rotor in the wind tunnel shows that the switching between the operating modes and the associated ~~tilting~~ of the spanwise angle of attack distribution works similar as to the full-scale rotor which fulfils one of the
570 major scaling objectives. In the measurements, the spanwise change in the axial induction distribution is smeared out which can not be reproduced by the inherent model assumptions of the BEM simulations. Complex flow structures were identified as an increased radial flow in the rotor plane and an additional vortex system that sheds from the blending region on the blade. Here, the question arises how the scaling effects the rotational augmentation and the radial flow components in the rotor plane, since the Rossby number (ratio of inertia to Coriolis forces) is not matched in the given scaling approach. Further, the local
575 blade solidity is increased for the model turbine which can further enhance the effect of rotational augmentation compared to the full-scale rotor (Herráez et al., 2016). However, FVW simulations for the full-scale turbines do confirm that the radial flow component is increased for the Hybrid-Lambda turbine compared to the reference turbine in a similar manner as shown in this paper for the model turbine. Further, the additional vortex system is also found in the full-scale simulations. Full insights to the complex flow phenomena on the blade and the impact of the scaling approach could only be revealed by blade resolved CFD
580 simulations which is out of the scope of this study.

Furthermore, the wind tunnel model allowed to reveal the unique wake characteristics of the Hybrid-Lambda Rotor and to underline three major advantages in the wake behaviour: First, the decreased wake deficits in the strong-wind mode, second, the increased wind speed in the outer wake annulus in the entire partial load range and third, the additional shear layer and
585 vortex system. To the authors knowledge, such a blade design with radially variable axial induction was never investigated in a wind tunnel before, which includes the ability to change the operating mode by changing the operational TSR, tilting the spanwise angle of attack distribution and reducing the axial induction. The major findings in this paper underline that the Hybrid-Lambda design methodology works reasonably, but designing a blade with such strong gradients along the blade span must be considered critically. This was somehow expected, since the first version of the Hybrid-Lambda Rotor was designed
590 in order to separate the effects on the inner and outer part of the blade and to push the limits of the applicability of the BEM theory where the blade elements are treated independently.

These findings are in line with previous FVW and LES investigations on the full-scale Hybrid-Lambda Rotor by Ribnitzky et al. (2023). A smearing of the gradients in the axial induction distribution was also recognised in the FVW investigations. Fur-
595 ther, the difference of the axial induction between the inner and the outer part of the blade was found to be reduced compared

to the BEM simulations. And finally, the wake characteristics are in very good agreement between the measurements presented in this paper and the aforementioned FVW and LES simulations on the full-scale rotor. The feature of the outer wake annulus with increased wind speeds and the resulting effects on the downstream flow structures are very similar across the simulations and the measurements. It was further found with both methods that the gradients in the wake profile smear out with increasing

600 turbulence intensity. Paulsen et al. (2024) investigated the Hybrid-Lambda Rotor using meso-scale weather research models. They showed that the benefits in a wind farm application even outperform those of the single turbine due to the reduced wake losses.

When we compare the hot-wire measurements in the wake with the LDA measurements in the rotor plane, we discover

605 some discrepancies. The gradients in the axial induction seem to be smeared out when considering the LDA data. But the wake profiles recorded with the hot-wires reveal a relatively steep gradient in the velocity profiles. This leads us to the limitations of the applied method, which aims for deriving the axial induction in the rotor plane by probing the wind speed in the bisectrix of two blades. According to Herráez et al. (2018), ideally, the induction of the rotor blades is counterbalanced and the velocities extracted from the rotor plane are just influenced by the wake induction and not by the blade induction itself.

610 However, this method cannot capture the influence of the local trailed and shed vorticities accurately. This applies usually to the tip region ($r/R > 0.92$) where the tip vortex starts to dominate the flow. In the present study, we found a second vortex system that emerges from the blending region on the blade and that will influence the circulation distribution along the blade span. Consequently, the LDA measurements close to the design blending region are also influenced by the additional vortex and those results should be treated with care. Since the vortex emerges from the blade, the LDA does not record steep gradients

615 in the rotor plane. Only with some downstream distance, the vortex leads to the sharp velocity gradients which can be captured with the hot-wires in the wake. Considering the outwards bending of the streamlines in Fig. 11 we can conclude that the inner wake core with the slower flow expands and pushes into the outer wake annulus. Consequently, the steep gradients in the wake profiles seem to develop within the first $0.5 D$ downstream of the rotor. This can somehow link the low gradients from the LDA measurements in the rotor plane to the steep gradients from the hot-wire data in the wake. Nevertheless, more measurements

620 in the direct proximity of the rotor with both measurement techniques would be necessary to underline this thesis. Despite the methodological limitations, the overall results and the combination of the hot-wire measurements in the wake with the FVW simulations give a good representation of the bigger picture concerning the flow structures of the Hybrid-Lambda Rotor.

In this paper, we focused on aerodynamic effects and steady-state operation. In a full-scale application, a reliable and

625 save operation of offshore low-specific-rating turbines with such large rotors can only be achieved with sophisticated control strategies. Specifically for the Hybrid-Lambda Rotor, the controller development should aim on realizing the transient change of operating modes and applying extreme load limiting techniques. The scaled model presented here offers the opportunity to test different controller versions under various reproducible turbulent inflow conditions in the wind tunnel which will be addressed in future studies.

6 Conclusions

In this paper, we first developed a method ~~on how~~ to scale the Hybrid-Lambda Rotor to wind tunnel size. Second, we investigated the influence of the steep gradients of axial induction along the blade span on the rotor aerodynamics. And third, we thoroughly analysed the wake characteristics of the Hybrid-Lambda Rotor and compared it to those of a conventional model rotor. We ~~learned~~ that it is possible to transfer a complex rotor concept to wind tunnel size and to lower design TSRs. In this delicate process of compromise finding, it is necessary to precisely define the scaling objectives. In this case we aimed for matching the axial induction distribution and to reproduce the shift in the angle of attack distribution when switching between the operating modes.

With the experimental investigations in the wind tunnel, we analysed the impact of the steep spanwise gradients in the blade design which lead to a complex three-dimensional flow. We found an additional shear layer and vortex system in the wake of the Hybrid-Lambda Rotor and we quantified the reduced wake deficits in the strong-wind mode and at rated conditions. Further, we tested the Hybrid-Lambda Rotor in gust events and the results show that the low-induction design of the outer part of the blade is beneficial and reduces the load overshoot by more than 4% compared to the conventional model turbine. The derived results help to understand the three-dimensional flow patterns that are introduced by the Hybrid-Lambda Rotor concept and provide a valuable complementary data set to the simulations on the full-scale rotor, as described by Ribnitzky et al. (2024). Further, the developed methodology can offer new inspirations when solving other scaling problems for complex wind turbine systems.

The successful experimental validation of the aerodynamic concept of the Hybrid-Lambda Rotor, so far on wind tunnel scale, confirms the prospect of deploying low-specific-rating turbines at exposed offshore sites. This can favour a higher and less fluctuating power feed-in at low to medium wind speeds. ~~Thus,~~ contributing to the transition to a reliable and economically reasonable supply ~~with~~ wind energy. Load limiting strategies are necessary to enable rotors with such large diameters and the accompanying losses in efficiency must be carefully considered within the design process. The Hybrid-Lambda Rotor can offer a possible solution and with the experimental work presented here, we ~~make~~ the next step in the concept validation.

Author contributions. DR developed the scaling methodology, designed the Hybrid-Lambda model turbine blades, conducted the experiments and simulations, post-processed the data and wrote the paper, VP supervised the experiments and the post-processing, MK contributed with effective discussions to the scaling methodology and to the blade design and supervised the investigations. All co-authors thoroughly reviewed the paper.

Competing interests. The contact author has declared that none of the authors has any competing interests.

660 *Acknowledgements.* We would like to thank Lars Neuhaus and Tom Wester for the support during the measurements. The work presented in this paper was funded by the Deutsche Forschungsgemeinschaft (DFG, German Research Foundation) – Project-ID 434502799 – SFB 1463.

References

Bayati, I., Belloli, M., Bernini, L., Mikkelsen, R., and Zasso, A.: On the aero-elastic design of the DTU 10MW wind turbine blade for the LIFES50+ wind tunnel scale model, Journal of Physics: Conference Series, 753, 022 028, https://doi.org/10.1088/1742-6596/753/2/022028, 2016.

Berger, F.: Wind tunnel experiments with a model turbine: Dynamic inflow investigation: Dissertation, https://oops.uni-oldenburg.de/id/eprint/5516, 2022.

Berger, F., Kröger, L., Onnen, D., Petrović, V., and Kühn, M.: Scaled wind turbine setup in a turbulent wind tunnel, Journal of Physics: Conference Series, 1104, 012 026, https://doi.org/10.1088/1742-6596/1104/1/012026, 2018.

Berger, F., Onnen, D., Schepers, G., and Kühn, M.: Experimental analysis of radially resolved dynamic inflow effects due to pitch steps, Wind Energy Science, 6, 1341–1361, https://doi.org/10.5194/wes-6-1341-2021, 2021.

Bottasso, C. L. and Campagnolo, F.: Wind Tunnel Testing of Wind Turbines and Farms. In: Stoevesandt, B., Schepers, G., Fuglsang, P., Yuping, S. (eds) Handbook of Wind Energy Aerodynamics, Springer, https://doi.org/10.1007/978-3-030-05455-7_54-1, 2021.

Bottasso, C. L., Campagnolo, F., and Petrović, V.: Wind tunnel testing of scaled wind turbine models: Beyond aerodynamics, Journal of Wind Engineering and Industrial Aerodynamics, 127, 11–28, https://doi.org/10.1016/j.jweia.2014.01.009, 2014.

Branlard, E., Brownstein, I., Strom, B., Jonkman, J., Dana, S., and Baring-Gould, E. I.: A multipurpose lifting-line flow solver for arbitrary wind energy concepts, Wind Energy Science, 7, 455–467, https://doi.org/10.5194/wes-7-455-2022, 2022.

Buhl, L.: A New Empirical Relationship between Thrust Coefficient and Induction Factor for the Turbulent Windmill State, National Renewable Energy Laboratory, NREL/TP-500-36834, 2005.

Campagnolo, F., Petrović, V., Schreiber, J., Nanos, E. M., Croce, A., and Bottasso, C. L.: Wind tunnel testing of a closed-loop wake deflection controller for wind farm power maximization, Journal of Physics: Conference Series, 753, 032 006, https://doi.org/10.1088/1742-6596/753/3/032006, 2016.

Canet, H., Bortolotti, P., and Bottasso, C. L.: On the scaling of wind turbine rotors, Wind Energy Science, 6, 601–626, https://doi.org/10.5194/wes-6-601-2021, 2021.

Dong, G., Qin, J., Li, Z., and Yang, X.: Characteristics of wind turbine wakes for different blade designs, Journal of Fluid Mechanics, 965, https://doi.org/10.1017/jfm.2023.385, 2023.

Dörenkämper, M., Meyer, T., Baumgärtner, D., Borowski, J., Deters, C., Dietrich, E., Fricke, J., Hans, F., Jersch, T., Leimeister, M., Neshati, M. M., Pangalos, G., Quiroz López, T. E., Quistorf, G., Requate, N., Schalk, K. V., Schmidt, J., Schnackenberg, M., Schwegmann, S., Thomas, P., Vollmer, L., Walgern, J., Widerspan, V., and Zotieieva, H.: Weiterentwicklung der Rahmenbedingungen zur Planung von Windenergieanlagen auf See und Netzanbindungssystemen, Fraunhofer-Institut für Windenergiesysteme, https://doi.org/10.24406/publica-2202, 2023.

Fontanella, A., Bayati, I., Mikkelsen, R., Belloli, M., and Zasso, A.: UNAFLOW: a holistic wind tunnel experiment about the aerodynamic response of floating wind turbines under imposed surge motion, Wind Energy Science, 6, 1169–1190, https://doi.org/10.5194/wes-6-1169-2021, 2021.

Gasch, R. and Twele, J.: Wind Power Plants: Fundamentals, Design, Construction and Operation, Springer, Berlin, 2nd edn., ISBN 978-3-642-22937-4, 2012.

Giguere, P. and Selig, M. S.: New Airfoils for Small Horizontal Axis Wind Turbines, ASME Journal of Solar Energy Engineering 120, pp. 108–114, 1998.

Hand, M. M., Simms, D. A., Fingersh, L. J., Jager, D. W., Cotrell, J. R., Schreck, S., and Larwood, S. M.: Unsteady Aerodynamics Experiment
700   Phase VI: Wind Tunnel Test Configurations and Available Data Campaigns, National Renewable Energy Laboratory NREL/TP-500-
        29955, 2001.

Hansen, M.: Aerodynamics of wind turbines, Earthscan, London, 2nd edn., ISBN 978-1-84407-438-9, 2008.

Herráez, I., Akay, B., van Bussel, G. J. W., Peinke, J., and Stoevesandt, B.: Detailed analysis of the blade root flow of a horizontal axis wind
        turbine, Wind Energy Science, 1, 89–100, https://doi.org/10.5194/wes-1-89-2016, 2016.

705   Herráez, I., Daniele, E., and Schepers, J. G.: Extraction of the wake induction and angle of attack on rotating wind turbine blades from PIV
        and CFD results, Wind Energy Science, 3, 1–9, https://doi.org/10.5194/wes-3-1-2018, 2018.

Hulskamp, A. W., van Wingerden, J. W., Barlas, T., Champliaud, H., van Kuik, G. A. M., Bersee, H. E. N., and Verhaegen, M.: Design of a
        scaled wind turbine with a smart rotor for dynamic load control experiments, Wind Energy, 14, 339–354, https://doi.org/10.1002/we.424,
        2011.

710   IEC 61400-1: Wind energy generation systems - Part 1: Design requirements, International Electrotechnical Commission, ed. 4, 2019.

Jonkman, B., Mudafort, R., Platt, A., Branlard, E., Sprague, M., Vijayakumar, G., Buhl, M., Ross, H., Bortolotti, P., Masciola, M., Ananthan,
        D., Schmidt, M., Rood, J., Hall, M., Bendl, K., and Martinez, T.: OpenFAST release v3.1.0, https://doi.org/10.5281/zenodo.6324288,
        2022.

Jonkman, J. and Sprague, M.: OpenFAST Documentation Release v3.1.0, National Renewable Energy Laboratory, Golden (US), 2021.

715   Jonkman, J., Butterfield, S., Musial, W., and Scott, G.: Definition of a 5-MW Reference Wind Turbine for Offshore System Development,
        National Renewable Energy Laboratory, NREL/TP-500-38060, 2009.

Kelley, C., Maniaci, D., and Resor, B.: Horizontal-Axis Wind Turbine Wake Sensitivity to Different Blade Load Distributions, AIAA SciTech,
        SAND2014-20587C, https://doi.org/10.2514/6.2015-0490, 2014.

Knauer, A.: Rotor blade shaped to enhance wake diffusion: European patent, EP 3 308 014 B1, 2021.

720   Kröger, L., Frederik, J., van Wingerden, J.-W., Peinke, J., and Hölling, M.: Generation of user defined turbulent inflow conditions by an active
        grid for validation experiments, Journal of Physics: Conference Series, 1037, 052 002, https://doi.org/10.1088/1742-6596/1037/5/052002,
        2018.

Krogstad, P. Å. and Lund, J. A.: An experimental and numerical study of the performance of a model turbine, Wind Energy, 15, 443–457,
        https://doi.org/10.1002/we.482, 2012.

725   López Prol, J., Steininger, K. W., and Zilberman, D.: The cannibalization effect of wind and solar in the California wholesale electricity
        market, Energy Economics, 85, 104 552, https://doi.org/10.1016/j.eneco.2019.104552, 2020.

Madsen, H. A., Zahle, F., Meng, F., Barlas, T., Rasmussen, F., and Rudolf, R. T.: Initial performance and load analysis of the LowWind
        turbine in comparison with a conventional turbine, Journal of Physics: Conference Series, 1618, 032 011, https://doi.org/10.1088/1742-
        6596/1618/3/032011, 2020.

730   May, N., Heuhoff, K., and Borggrefe, F.: Market incentives for system-friendly designs of wind turbines, DIW Economic Bulletin No.
        24/2015, pp. 313–321, 2015.

Neuhaus, L., Berger, F., Peinke, J., and Hölling, M.: Exploring the capabilities of active grids, Experiments in Fluids, 62, 130,
        https://doi.org/10.1007/s00348-021-03224-5, 2021.

Paulsen, J., Dörenkämper, M., and Steinfeld, G.: Power production and large-scale wake effects of offshore wind turbines with low specific
735   rating, Journal of Physics: Conference Series, 2767, 092 060, https://doi.org/10.1088/1742-6596/2767/9/092060, 2024.

Ribnitzky, D., Berger, F., and Kühn, M.: Innovative aerodynamic rotor concept for demand-oriented power feed-in of offshore wind turbines, Journal of Physics: Conference Series, 2265, 032 017, https://doi.org/10.1088/1742-6596/2265/3/032017, 2022.

Ribnitzky, D., Bortolotti, P., Branlard, E., and Kühn, M.: Rotor and wake aerodynamic analysis of the Hybrid-Lambda concept - an offshore low-specific-rating rotor concept, Journal of Physics: Conference Series, 2626, 012 008, https://doi.org/10.1088/1742-6596/2626/1/012008, 2023.

Ribnitzky, D., Berger, F., Petrović, V., and Kühn, M.: Hybrid-Lambda: a low-specific-rating rotor concept for offshore wind turbines, Wind Energy Science, 9, 359–383, https://doi.org/10.5194/wes-9-359-2024, 2024.

Schepers, J. P. and Snel, H.: Model Experiments in Controlled Conditions - Final Report, Energy research Center of the Netherlands (ECN), Tech. rep. ECN-E-07-042, Petten, 2008.

Schneemann, J., Rott, A., Dörenkämper, M., Steinfeld, G., and Kühn, M.: Cluster wakes impact on a far-distant offshore wind farm's power, Wind Energy Science, 5, 29–49, https://doi.org/10.5194/wes-5-29-2020, 2020.

Schottler, J., Hölling, A., Peinke, J., and Hölling, M.: Design and implementation of a controllable model wind turbine for experimental studies, Journal of Physics: Conference Series, 753, 072 030, https://doi.org/10.1088/1742-6596/753/7/072030, 2016.

Shaler, K., Branlard, E., and Platt, A.: OLAF User's Guide and Theory Manual, National Renewable Energy Laboratory, NREL/TP-5000-75959, https://doi.org/10.2172/1659853, 2020.

Soto-Valle, R., Bartholomay, S., Alber, J., Manolesos, M., Nayeri, C. N., and Paschereit, C. O.: Determination of the angle of attack on a research wind turbine rotor blade using surface pressure measurements, Wind Energy Science, 5, 1771–1792, https://doi.org/10.5194/wes-5-1771-2020, 2020.

Swisher, P., Murcia Leon, J. P., Gea-Bermúdez, J., Koivisto, M., Madsen, H. A., and Münster, M.: Competitiveness of a low specific power, low cut-out wind speed wind turbine in North and Central Europe towards 2050, Applied Energy, 306, 118 043, https://doi.org/10.1016/j.apenergy.2021.118043, 2022.

Wang, C., Campagnolo, F., Canet, H., Barreiro, D. J., and Bottasso, C. L.: How realistic are the wakes of scaled wind turbine models?, Wind Energy Science, 6, 961–981, https://doi.org/10.5194/wes-6-961-2021, 2021.

Yang, X., Boomsma, A., Sotiropoulos, F., Resor, B., Maniaci, D., and Kelley, C.: Effects of spanwise blade load distribution on wind turbine wake evolution, AIAA SciTech 2015-0492, https://doi.org/10.2514/6.2015-0492, 2015.